

# Synthesis and photocatalytic application of visible-light active $\beta\text{-Fe}_2\text{O}_3/\text{g-C}_3\text{N}_4$ hybrid nanocomposites

Konstantinos C. Christoforidis <sup>a,\*</sup>, Tiziano Montini <sup>a</sup>, Elza Bontempi <sup>b</sup>, Spyridon Zafeiratos <sup>c</sup>, Juan José Delgado Jaén <sup>d</sup>, Paolo Fornasiero <sup>a,\*</sup>

<sup>a</sup> Department of Chemical and Pharmaceutical Sciences, ICCOM-CNR Trieste Research Unit—INSTM Research Unit, University of Trieste, via L. Giorgieri 1, 34127 Trieste, Italy

<sup>b</sup> Chemistry for Technologies Laboratory and INSTM, Department of Mechanical and Industrial Engineering, University of Brescia, via Branze 38, Brescia, Italy

<sup>c</sup> Institut de Chimie et Procédés Pour l'Energie, l'Environnement et la Santé, (ICPEES) ECPM, University of Strasbourg, 25 rue Becquerel Cedex 2, 67087 Strasbourg, France

<sup>d</sup> Departamento de Ciencia de los Materiales e Ingeniería Metalúrgica y Química Inorgánica, Facultad de Ciencias, Universidad de Cádiz, Campus Río San Pedro, 11510, Puerto Real, Cádiz, Spain

## ARTICLE INFO

Accepted 9 January 2016

**Keywords:**  
 $\beta\text{-Fe}_2\text{O}_3$   
 $\text{g-C}_3\text{N}_4$   
Heterojunction  
Hybrid  
Composite  
Photocatalysis

## ABSTRACT

Hybrid organic/inorganic nanocomposites comprised of nanocrystalline iron oxide at the metastable  $\beta$ -phase and graphitic carbon nitride ( $\text{g-C}_3\text{N}_4$ ) were prepared via a facile *in-situ* growth strategy embedded in a solid state process. The hybridized  $\beta\text{-Fe}_2\text{O}_3/\text{g-C}_3\text{N}_4$  nanomaterials were thoroughly characterized by a variety of techniques, including UV-vis absorption, nitrogen physisorption, X-ray diffraction (XRD), Fourier transform infrared spectroscopy (FT-IR) and transmission electron microscopy (TEM). Their photocatalytic activity was evaluated under both simulated solar light and pure visible light irradiation against the photodegradation of methyl orange (MO), rhodamine B (RhB) and phenol. The prepared  $\beta\text{-Fe}_2\text{O}_3/\text{g-C}_3\text{N}_4$  nanocomposites were proven durable and significantly more efficient than the single components. The  $\beta\text{-Fe}_2\text{O}_3$  content in the final material was tuned to optimize the photocatalytic performance, with particular attention to the activity under visible light. The enhanced photoactivity was attributed to a) the improved optical properties of the prepared nanocomposites, presenting narrower band-gap energies and increased visible light absorption efficiency, and b) to the efficient separation of the photoinduced charge carriers driven by the matched band edges in the heterostructure. The predominant active species responsible for the photodegradation activity were determined and a possible mechanism is proposed.

## 1. Introduction

Over the last decades, photocatalysis using semiconductor materials and solar energy as the energy source has been established as an attractive method for environmental protection and energy production [1]. A variety of transition metal oxides, pure and their doped derivatives [2,3], including expensive precious metals [4,5], metal sulfides [6,7], and hybrid nanocomposites [8,9] have been prepared and evaluated. High cost, complicated synthesis process, fast electron-hole recombination, dissolved metal ions and limited activity under visible light of the photocatalyst materials are considered the barriers for the wide application of

photocatalysis in environmental remediation. Ti-based materials occupy the vast majority of the applied materials in photocatalytic degradation reactions in the gas or liquid phase [2]. However,  $\text{TiO}_2$ , being a wide band gap semiconductor ( $\sim 3.2$  eV for anatase) [10], has no response to visible light. Therefore, the development of stable, environmental-friendly and efficient photocatalysts under solar light irradiation is still a significant challenge for realistic applications.

Recently, the polymeric semiconductor graphite-like carbon nitride ( $\text{g-C}_3\text{N}_4$ ) has stimulated scientists' interest in photo-triggered reactions. The unique properties of  $\text{g-C}_3\text{N}_4$ , having a 2-dimensional metal-free structure containing only carbon and nitrogen, the excellent chemical and thermal stability, low cost, simple synthesis process and relatively narrow band gap energy ( $\sim 2.7$  eV) established it as a promising material for practical photocatalytic applications making use of solar energy [11,12]. However, pure  $\text{g-C}_3\text{N}_4$  suffers from fast recombination rates of the

\* Corresponding authors.

E-mail addresses: [kchristoforidis@units.it](mailto:kchristoforidis@units.it) (K.C. Christoforidis), [p.fornasiero@units.it](mailto:p.fornasiero@units.it) (P. Fornasiero).

photogenerated charge carries (electron/hole pairs,  $e^-/h^+$ ) and small specific surface area [11]. Therefore, improvements are required to eliminate the inherent drawbacks. Efforts to improve the photocatalytic activity of g-C<sub>3</sub>N<sub>4</sub> include doping with metallic [13–16] and non-metallic elements [17–19], increase of the specific surface area [20,21], functionalization with metal nanoparticles [22,23], control of morphology [24–26] as well as development of composites and heterostructures [14,27–34]. In addition, it has been documented that factors such as the organic precursor (melamine, urea etc.) and the actual conditions of the thermal treatment (i.e. temperature, atmosphere) used for the preparation of g-C<sub>3</sub>N<sub>4</sub> greatly affect the activity of such photocatalysts [35–37]. Therefore, different catalytic activities have been reported for materials prepared *via* different roots.

From the different approaches applied to enhance the activity of g-C<sub>3</sub>N<sub>4</sub>, coupling with other semiconductors is particularly interesting. The coupling of different semiconductors and the formation of nanocomposites based on abundantly available raw materials, presenting unique properties not found in the individual compounds, is an ideal process for the development of cheap materials with advanced properties. Composite materials of g-C<sub>3</sub>N<sub>4</sub> coupled with different metal oxides has been shown to enhance  $e^-/h^+$  separation and increase light absorption in the visible region, presenting superior photocatalytic activity than the pure g-C<sub>3</sub>N<sub>4</sub> [14,27,38–41]. This strategy is mainly focused on the efficient separation of the photogenerated charge carriers *via* selecting oxides with energetically matching conduction (CB) and valence bands (VB) with respect to g-C<sub>3</sub>N<sub>4</sub>, offering the appropriate driving force for efficient charge transfer and separation.

Iron oxides are non-toxic, cheap and abundant, presenting relatively small band gap energies capable to absorb visible light. However, single iron oxides present normally low photocatalytic activity caused by the rapid recombination of photo-induced charge carriers [42]. Control of the morphology at the nanoscale may improve the recombination processes. Of the different polymorphs of ferric oxide (Fe<sub>2</sub>O<sub>3</sub>), the  $\alpha$ - and  $\gamma$ -phases are the most frequently studied. The  $\beta$ -Fe<sub>2</sub>O<sub>3</sub> and  $\varepsilon$ -Fe<sub>2</sub>O<sub>3</sub> polymorphs have been scarcely investigated since it is difficult to prepare them as single phase materials [43,44]. Particularly the  $\beta$ -Fe<sub>2</sub>O<sub>3</sub>, which is a metastable phase during the formation of  $\alpha$ -Fe<sub>2</sub>O<sub>3</sub>, is considered rather unstable under thermal treatments. Nevertheless, recently  $\beta$ -Fe<sub>2</sub>O<sub>3</sub> and  $\varepsilon$ -Fe<sub>2</sub>O<sub>3</sub> prepared *via* chemical vapor deposition method have been efficiently applied in photo-initiated reactions for H<sub>2</sub> production [45,46].

Very recently, g-C<sub>3</sub>N<sub>4</sub> coupled with iron oxides ( $\alpha$ -Fe<sub>2</sub>O<sub>3</sub>,  $\gamma$ -Fe<sub>2</sub>O<sub>3</sub> and Fe<sub>3</sub>O<sub>4</sub>) have been prepared and applied for the photodegradation of model pollutants [14,27,38,47,48]. Iron-modified g-C<sub>3</sub>N<sub>4</sub> based photocatalysts have been also effectively applied for selective organic synthesis reactions [49,50]. Different approaches have been adopted for their preparation including *in-situ* as well as two-step processes, solution chemistry and hydrothermal treatments. Considering the demonstrated potential of both Fe<sub>2</sub>O<sub>3</sub> and g-C<sub>3</sub>N<sub>4</sub> in many exciting photo-triggered applications in the field of sustainable energy production [11,42,45,46,51], water and air purification [14,27,38] and fine chemical production [49,50], together with their advantages over other photocatalysts, the development of simple and fast synthesis process towards the production of advanced materials based on Fe<sub>2</sub>O<sub>3</sub> and g-C<sub>3</sub>N<sub>4</sub> is of great significance. Herein, a facile solid state process was applied for the growth of Fe<sub>2</sub>O<sub>3</sub> nanoparticles in the form of the metastable  $\beta$ -phase on the surface of g-C<sub>3</sub>N<sub>4</sub> by an *in-situ* growth strategy, without the need of specialized equipment, surfactants, stabilization or precipitating agents. The formation of the hybrid nanocomposites was verified by TEM, XRD and XPS. Small and well dispersed  $\beta$ -Fe<sub>2</sub>O<sub>3</sub> nanoparticles were overlaid on the surface of g-C<sub>3</sub>N<sub>4</sub>. A series of hybrid  $\beta$ -Fe<sub>2</sub>O<sub>3</sub>/g-C<sub>3</sub>N<sub>4</sub> nanocomposites with

different iron oxide content was obtained. The prepared materials were characterized and their photocatalytic activity was evaluated against the degradation of organic dyes (MO and RhB) and phenol under both artificial solar light and pure visible light irradiation. The nanohybrids were found more active than the pure g-C<sub>3</sub>N<sub>4</sub> and  $\beta$ -Fe<sub>2</sub>O<sub>3</sub> materials. Reference reactions in the presence of various scavengers were carried out and the predominant active species were unambiguously determined. The photocatalytic mechanism was tentatively proposed based on the band-structure of the hybrid materials.

## 2. Experimental

Melamine, Fe(SO<sub>4</sub>)<sub>3</sub>, NaCl, Na<sub>2</sub>SO<sub>4</sub>, methyl orange (MO), rhodamine B (RhB), phenol and triethanolamine (TEOA) were purchased from Sigma-Aldrich. *Tert*-butyl alcohol (TBA) was purchased from Fluka. All chemicals were of analytical grade and used without any further purification.

### 2.1. Materials synthesis

Graphitic carbon nitride was synthesized via thermal polycondensation of melamine [52]. Melamine was put into analumina crucible with a cover and heated in air at 550 °C in a muffle furnace for 4 h with a heating rate of 5 °C min<sup>-1</sup>. The yellow material was collected, rinsed with 0.1 M HNO<sub>3</sub> to remove any remaining NH<sub>3</sub> and washed thoroughly with double-distilled water. Finally, it was dried over night at 100 °C and ground into fine powder for further use.

The  $\beta$ -Fe<sub>2</sub>O<sub>3</sub>/g-C<sub>3</sub>N<sub>4</sub> nanocomposites were synthesized using a solid state process. First, NaFe(SO<sub>4</sub>)<sub>2</sub> salt was obtained as the iron precursor [43]. A 20 ml aqueous solution containing Fe(SO<sub>4</sub>)<sub>3</sub> and NaSO<sub>4</sub> at a 1:1 molar ratio was stirred for 1 h. Then, water was evaporated and the light brown salt was collected. For the synthesis of the hybrid materials, NaFe(SO<sub>4</sub>)<sub>2</sub> and NaCl with a 1:8 molar ratio were thoroughly mixed with an agate mortar. 0.123 g of NaFe(SO<sub>4</sub>)<sub>2</sub> were used to prepare the FCN-3 sample. Then, g-C<sub>3</sub>N<sub>4</sub> (0.6 g) was added and the three components were further thoroughly mixed for 30 min with an agate mortar. The mixture was placed in an alumina crucible and heated in air at 500 °C for 1 h with a heating rate of 3 °C min<sup>-1</sup>. The materials were collected, washed thoroughly with double-distilled water and acetone *via* filtration to remove the remaining of the metal salt used, dried at 100 °C overnight and finally grounded into powders. By varying the amount of the NaFe(SO<sub>4</sub>)<sub>2</sub>/NaCl mixture, materials with different iron content were prepared. The color of the hybrid materials changed from yellow to orange and light brown with increasing iron content. Pure  $\beta$ -Fe<sub>2</sub>O<sub>3</sub> was synthesized in a similar way in the absence of g-C<sub>3</sub>N<sub>4</sub>. The hybrid materials are labeled FCN-x where the increasing x value denotes samples with increasing Fe content. The Fe content ranged within 1.6–7.1 wt% according to TGA analysis (see in the following). CN stands for the pure g-C<sub>3</sub>N<sub>4</sub> sample. A mechanically mixed sample (MFCN-4) containing similar Fe-content as the FCN-4 according to TGA analysis was also prepared.

### 2.2. Characterization

Thermogravimetric analysis (TGA) was performed with a TGA Q500 (TA Instruments) under air flow, from 100 to 800 °C with a heating rate of 10 °C min<sup>-1</sup>. The composition of the nanocomposites was calculated from the weight difference between 200 and 700 °C. Nitrogen adsorption-desorption isotherms were obtained at the liquid nitrogen temperature using a Micrometrics ASAP2020 system. Each sample was degassed at 170 °C overnight and the Brunauer-Emmett-Teller (BET) model was used to determine the specific surface area. Fourier transform infrared (FT-IR) spectra in

the 4000–400 cm<sup>-1</sup> region were recorded using KBr pellets with a Perkin Elmer 2000 instrument. TEM measurements were performed on a TEM Philips EM208, using an acceleration voltage of 100 kV. Samples were prepared by drop casting onto a TEM grid (200 mesh, copper, carbon only). High Resolution Transmission Electron Microscopy (HRTEM) images were recorded by a JEOL 2010-FEG microscope operating at the acceleration voltage of 200 kV. The microscope has 0.19 nm spatial resolution at Scherzer defocus conditions in HRTEM mode. X-ray diffraction (XRD) spectra were collected in reflection mode on a D/Max-RAPID X-ray microdiffractometer with a cylindrical imaging plate detector, using CuK $\alpha$  radiation and a collimator diameter of 300  $\mu$ m. Conventional XRD patterns were obtained by integration of bi-dimensional images. The X-ray photoelectron spectroscopy (XPS) measurements were carried out in an ultrahigh vacuum (UHV) spectrometer equipped with a VSW Class WA hemispherical electron analyzer. A monochromatic Al K $\alpha$  X-ray source (1486.6 eV) was used as incident radiation. Survey and high resolution spectra were recorded in constant pass energy mode (90 and 44 eV, respectively). UV-vis diffuse reflectance spectroscopy experiments were performed with a PerkinElmer (Lambda 35) spectrophotometer equipped with an integrating sphere assembly with a nominal resolution of 1 nm using BaSO<sub>4</sub> as reference. The band gap energies of the pure and FCN-x nanomaterials were estimated from their optical absorption edges using the following formula:

$$ahv = B(hv - E_g)^2$$

where  $hv$ ,  $\alpha$  and  $B$  represent the excitation energy, absorption coefficient and a constant, respectively. Instead of  $a$ , the Kubelka-Munk function was applied in order to eliminate any tailing contribution from the DR-UV-vis spectra [7,53]. The following function was applied to convert the absorption spectra:

$$F(R) = \frac{(1 - R)^2}{2R}$$

where  $R$  is the reflectance. The  $E_g$  values were estimated from the plot of  $F(R)hv^{1/2}$  versus energy by extrapolating the linear part.

### 2.3. Photocatalytic degradation

The photocatalytic activity of the prepared catalysts was evaluated against the degradation of MO, RhB and phenol (a recalcitrant pollutant) in aqueous solution. Catalytic tests were performed under simulated solar light (Solar simulator LOT-Oriel equipped with 300 W Xe Arc light source and AM 1.5 filter) and pure visible light using a 420 nm cut-off filter. The catalyst (1.25 g L<sup>-1</sup> for dyes and 2 g L<sup>-1</sup> for phenol) and 160 ml of aqueous solution containing 10 mg L<sup>-1</sup> of MO or RhB and 5 mg L<sup>-1</sup> of phenol were placed in a Teflon reactor and the reaction temperature was maintained at 20 °C. Prior to irradiation, the suspension was stirred for 1.5 h in the dark to reach the adsorption/desorption equilibrium. The adsorption under dark conditions never exceeded 14%. The catalytic results reported herein are after adsorption/desorption equilibrium was reached. To quantify MO and RhB, aliquots (2 ml) of the suspension were periodically taken and filtered using a 0.45  $\mu$ m PTFE Millipore disc. To quantify phenol, 3 ml aliquots were drawn and centrifuged at certain time intervals. A Shimadzu UV-2450 UV/Vis spectrometer was used to determine the concentration of dyes and phenol. Quantification was based on comparison with standards. To quantify the iron amount leached during photocatalytic experiments, the samples were filtrated using 0.45  $\mu$ m PTFE membranes and analyzed using inductively coupled plasma and atomic emission spectroscopy (ICP-AES). The Limit of Detection (LOD) at the used wavelength (238.204 nm) is  $\sim$ 10  $\mu$ g L<sup>-1</sup>. For the recycling experiments, the used catalyst was collected, washed with

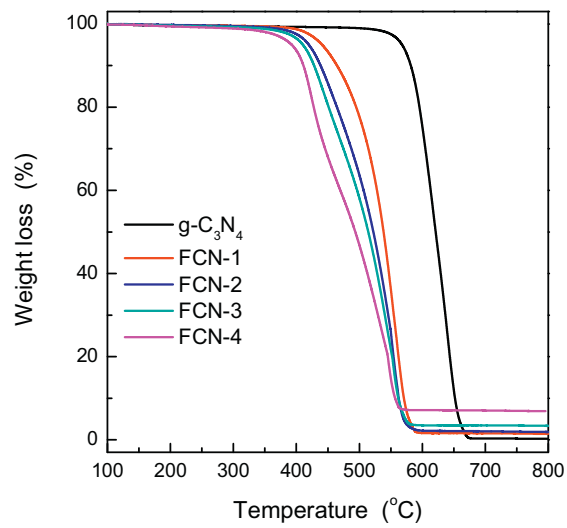


**Fig. 1.** TGA profiles of pure g-C<sub>3</sub>N<sub>4</sub> and the as-prepared  $\beta$ -Fe<sub>2</sub>O<sub>3</sub>/g-C<sub>3</sub>N<sub>4</sub> nanomaterials.

**Table 1**  
Characteristics of the prepared nanomaterials.

Sample	wt% $\beta$ -Fe <sub>2</sub> O <sub>3</sub> <sup>a</sup>	BET (m <sup>2</sup> /g)	Pore volume (cm <sup>3</sup> /g)	$E_g$ (eV)
CN	0	13.4	0.120	2.74
FCN-1	1.6	28.8	0.151	2.67
FCN-2	2.1	21.5	0.157	2.62
FCN-3	3.5	21.1	0.141	2.55
FCN-4	7.1	20.8	0.112	2.40
MFCN-4	7.0	11.0	0.089	2.73
$\beta$ -Fe <sub>2</sub> O <sub>3</sub>	100	2.1	0.008	1.77

<sup>a</sup> Calculated from the TGA profiles.

water three consecutive times under stirring, washed with acetone and finally dried over night at 100 °C. The mechanistic aspects of the catalytic reaction were studied by using scavengers. TEOA and TBA (0.1 mmol) were used as hole ( $h^+$ ) and hydroxyl radical ( $OH^\bullet$ ) scavengers, respectively. Argon was used to study the effect of superoxide radical ( $O_2^{-\bullet}$ ) formation on photoactivity.

## 3. Results and discussion

### 3.1. Characterization of photocatalysts

Thermogravimetric analysis was carried out to investigate the thermal stability and the composition of the prepared materials. Fig. 1 shows TGA profiles of the CN and the FCN-x samples. The pure CN sample begins to be oxidized at temperatures above 560 °C verifying that it is stable under the second thermal treatment at 500 °C. On the contrary, the FCN-x composites start to be oxidized at lower temperatures, thanks to a catalytic activation of oxygen associated to the presence of iron oxide. In fact, with increasing iron content the decomposition temperature decreases. The content of the  $\beta$ -Fe<sub>2</sub>O<sub>3</sub> in the hybrid materials was calculated from the remaining weight, as summarized in Table 1. Based on the TGA analysis, approximately half of the nominal Fe content is present in the final FCN-x composites, while the loss of the initial added Fe is higher for samples treated with higher Fe amount.

Fig. 2 shows XRD patterns of the pure and the hybrid materials. Both the pure g-C<sub>3</sub>N<sub>4</sub> and the FCN-x samples exhibit two characteristic reflections at approximately  $2\theta$  13.1° and 27.3° corresponding to the (1 0 0) and (0 0 2) crystal planes of g-C<sub>3</sub>N<sub>4</sub>. These two features confirmed the formation of the graphitic stacking structure via melamine's polycondensation at 550 °C. In addition, the XRD data provide direct evidence that the g-C<sub>3</sub>N<sub>4</sub> structure is not

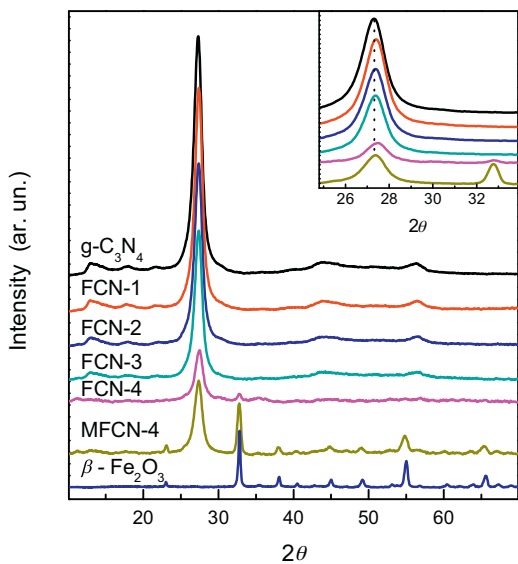


**Fig. 2.** XRD patterns of the pure  $\text{g-C}_3\text{N}_4$  and  $\beta\text{-Fe}_2\text{O}_3$  and the hybrid FCN-x and MFCM-4 nanomaterials. Inset: close view of the (002) reflection of the  $\text{g-C}_3\text{N}_4$ .

significantly altered by the additional thermal treatment at  $500^\circ\text{C}$  used during the preparation of the iron oxide. However, a gradual degrease of the main reflection intensity with increasing iron content is observed which has been previously observed and assigned to host-guest interaction [54]. Closer inspection of the data also reveals a shift towards higher  $2\theta$  values of the (0 0 2) reflection for all hybrid materials (about  $0.2^\circ$ , inset in Fig. 1). This shift was not detected in the mechanical mixed MFCM-4 sample. The loss of the intensity and the shift of the (0 0 2) diffraction peak clearly indicates an interaction between the organic and the inorganic part in the hybrid materials.

The XRD pattern of the pure iron oxide sample is also displayed in Fig. 2. The characteristic diffraction pattern can be fully indexed to the pure metastable  $\beta\text{-Fe}_2\text{O}_3$  phase [43]. The sharp reflections indicate high crystallinity. The pattern of  $\beta\text{-Fe}_2\text{O}_3$  is clearly observed also in the MFCM-4 sample. Vice versa, in the hybrid materials, only the main  $\beta\text{-Fe}_2\text{O}_3$  reflection at  $32.8^\circ$  is detected in the composite sample with the higher iron loading (FCN-4). No diffraction peaks attributed to other  $\text{Fe}_2\text{O}_3$  polymorph are observed. The absence of  $\beta\text{-Fe}_2\text{O}_3$  reflections in the nanocomposites is most likely due to the low amount of  $\text{Fe}_2\text{O}_3$  as evidenced

by TGA. In addition, it may also indicate that the oxide's nanoparticles are small and well dispersed on the  $\text{g-C}_3\text{N}_4$  surface, suggesting that the growth of the iron oxide nanoparticles is restrained in the presence of  $\text{g-C}_3\text{N}_4$ .

Fourier transform infrared (FT-IR) spectra of the  $\text{g-C}_3\text{N}_4$ ,  $\beta\text{-Fe}_2\text{O}_3$  and the hybrid materials are presented in Fig. 3. All characteristic peaks of  $\text{g-C}_3\text{N}_4$  were observed in the hybrid and the pure  $\text{g-C}_3\text{N}_4$  spectra. The broad absorption band at high wavenumber ( $\sim 3200\text{ cm}^{-1}$ ) is attributed to the stretching vibration of N–H bonds (primary ( $-\text{NH}_2$ ) and secondary ( $=\text{N}-\text{H}$ ) amines). The contribution of surface O–H groups is negligible in this region, considering that no bands have been observed even on the pure  $\beta\text{-Fe}_2\text{O}_3$  material. The multiple absorption bands in the  $1200\text{--}1680\text{ cm}^{-1}$  region originate from the stretching vibration modes of heptazine heterocyclic ring, typical for CN heterocycles. The sharp peaks at  $810\text{ cm}^{-1}$  originates from the breathing mode of the triazine units. The  $\text{g-C}_3\text{N}_4$  bands are present in the  $\beta\text{-Fe}_2\text{O}_3/\text{g-C}_3\text{N}_4$  which suggests that the  $\text{g-C}_3\text{N}_4$  structural features are maintained during the hybridization process, in agreement with XRD. The pure  $\beta\text{-Fe}_2\text{O}_3$  exhibited two main absorption peaks at approximately  $460$  and  $630\text{ cm}^{-1}$ , observed only slightly at the high-Fe loaded materials (FCN-4 and MFCN-4, Fig. 3B).

The surface composition of the pure  $\text{g-C}_3\text{N}_4$  and FCN-x nanocomposites was investigated by means of XPS spectroscopy. Fig. S1 shows XPS survey spectra of selected samples. The corresponding high-resolution XPS spectra of the C 1s, N 1s, and Fe 2p regions are presented in Fig. S2. The survey spectra indicate the presence of C, N and O on the surface of the pure  $\text{g-C}_3\text{N}_4$  and C, N, O and Fe on the  $\beta\text{-Fe}_2\text{O}_3/\text{g-C}_3\text{N}_4$  nanocomposites. The O 1s peak in the  $\text{g-C}_3\text{N}_4$  is assigned to adsorb  $\text{H}_2\text{O}$ . No peak of Na was detected in the narrow scan Na 1s spectra (not shown), indicating that doping of  $\text{g-C}_3\text{N}_4$  with Na did not take place under the conditions applied and no un-reacted metal salts remained after the washing treatment. Typical C 1s and N 1s XPS spectra were recorded for all samples. The main C 1s contribution centered at  $288.5\text{ eV}$  is ascribed to  $\text{C}(\text{N})_3$  while the main N 1s peak at  $398.9\text{ eV}$  can be attributed to  $\text{C}=\text{N}-\text{C}$   $\text{sp}^2$ -hybridized N-atoms. The Fe 2p<sub>3/2</sub> peak centered at  $711.2\text{ eV}$  is ascribed to the formation of  $\beta\text{-Fe}_2\text{O}_3$ . XPS data showed the presence of a single iron oxide species, indicating that Fe was not introduced at interstitial positions in the  $\text{g-C}_3\text{N}_4$  structure. The absence of both Na and Fe in the  $\text{g-C}_3\text{N}_4$  structure was expected since  $\text{g-C}_3\text{N}_4$  was pre-formed during the synthesis of the FCN-x nanocomposites.

Nitrogen physisorption isotherms (Fig. 4) were performed to study the textural properties of the materials. The hysteresis loop

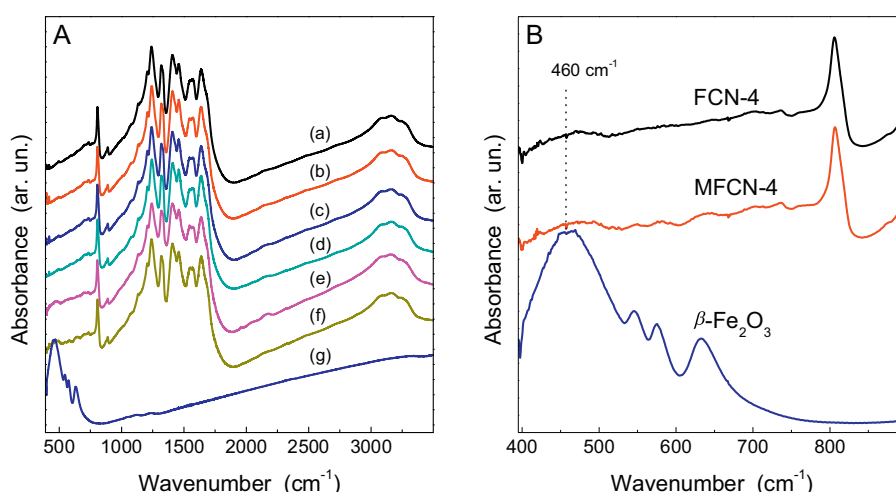


**Fig. 3.** (A) FT-IR absorption spectra of the  $\text{g-C}_3\text{N}_4$  (a),  $\beta\text{-Fe}_2\text{O}_3/\text{g-C}_3\text{N}_4$  (b)-(e), MFCM-4 (f) and  $\beta\text{-Fe}_2\text{O}_3$  (g) nanomaterials; (B) Detail in the  $400\text{--}900\text{ cm}^{-1}$  region.

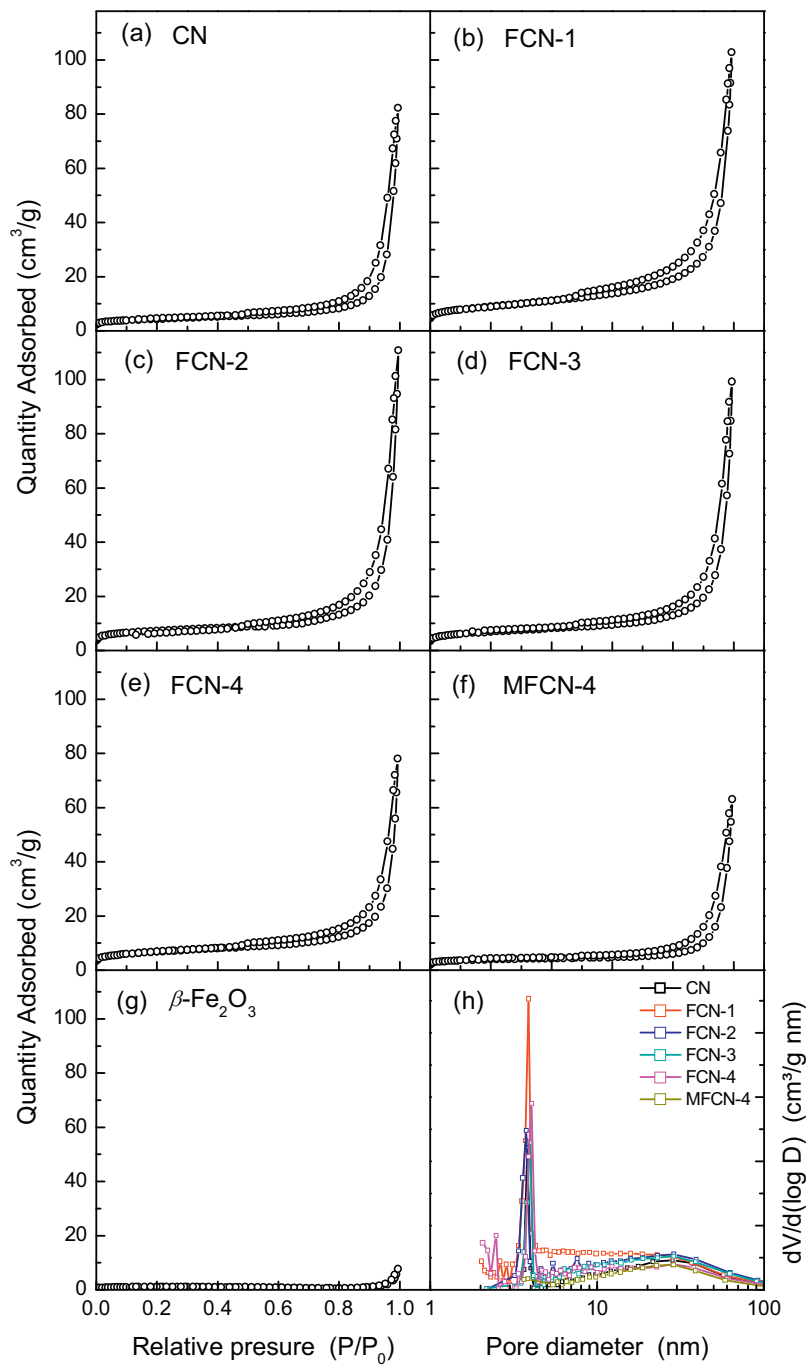


**Fig. 4.** Nitrogen physisorption isotherms (a-g) and pore size distribution (h) calculated from the desorption branch of the N<sub>2</sub> isotherm using the BJH method.

observed at relatively low partial pressures ( $0.4 < P/P_0 < 0.9$ ) can be attributed to the intra-aggregated pores and at higher partial pressures ( $0.9 < P/P_0 < 1$ ) to the large pores formed between secondary particles, typical for g-C<sub>3</sub>N<sub>4</sub>. The corresponding BJH pore-size distribution curves are presented in Fig. 4h. All samples presented a bimodal pore size distribution, with a main contribution in the range 3.5–4 nm and a second and broader centered at about 20–30 nm. Table 1 summarizes the textural properties of the nanocomposites and pure materials, along with other properties. An increase of the surface area was observed upon introducing β-Fe<sub>2</sub>O<sub>3</sub> in the g-C<sub>3</sub>N<sub>4</sub>. This increase was not observed for the mechanical mixed MFCN-4 sample.

Transmission electron microscopy (TEM) was used to study the morphology of the as-prepared g-C<sub>3</sub>N<sub>4</sub> and FCN-x hybrids.

Representative images are given in Fig. 5. High magnification TEM images are also displayed in Fig. S3. A typical layered and platelet-like structure is observed in the pure g-C<sub>3</sub>N<sub>4</sub> sample formed via the aggregation of irregular and varying size particles. The layered structure is preserved in the hybrid materials. Nevertheless, comparing the hybrid materials with the pure g-C<sub>3</sub>N<sub>4</sub> a decrease on the layer's size was observed. This can explain the higher surface area of the FCN-x samples compared with the pure g-C<sub>3</sub>N<sub>4</sub> (Table 1). In the FCN-x series, well dispersed oxide nanoparticles are overlaid on the surface of g-C<sub>3</sub>N<sub>4</sub> (Fig. 7B, C and S3A). The average size of such nanoparticles is around 3.5 nm. The small sized and highly dispersed β-Fe<sub>2</sub>O<sub>3</sub> nanoparticles observed in the β-Fe<sub>2</sub>O<sub>3</sub>/g-C<sub>3</sub>N<sub>4</sub> nanomaterials explain the inability to detect the oxide with XRD. No free β-Fe<sub>2</sub>O<sub>3</sub> nanoparticles were detected outside of the g-C<sub>3</sub>N<sub>4</sub>.

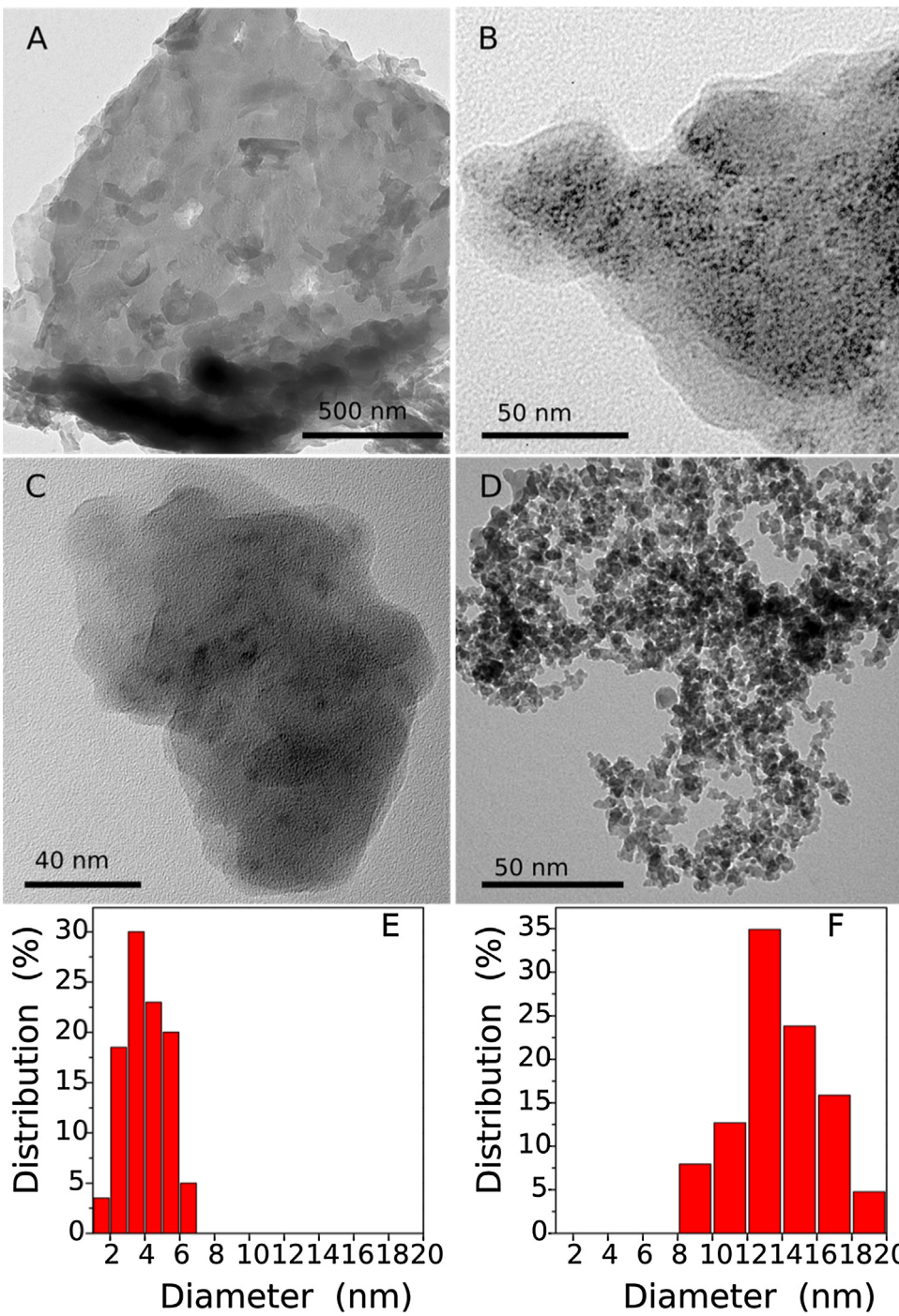


**Fig. 5.** TEM images of the  $\text{g-C}_3\text{N}_4$  (A), FCN-3 (B), FCN-4 (C), the pure  $\beta\text{-Fe}_2\text{O}_3$  (D) and the  $\beta\text{-Fe}_2\text{O}_3$  particle size distribution in the FCN-3 (E) and the  $\beta\text{-Fe}_2\text{O}_3$  (F) sample.

sheets. On the contrary, the pure  $\beta\text{-Fe}_2\text{O}_3$  presented an average particle size of 13 nm (Fig. 5D and S3C). These results clearly indicate that the *in-situ* growth of  $\beta\text{-Fe}_2\text{O}_3$  on the surface of  $\text{g-C}_3\text{N}_4$  applied for the synthesis of the  $\beta\text{-Fe}_2\text{O}_3/\text{g-C}_3\text{N}_4$  hybrids results in significantly smaller  $\beta\text{-Fe}_2\text{O}_3$  nanoparticles, at the same time avoiding the formation of  $\beta\text{-Fe}_2\text{O}_3$  agglomerates. The lattice fringe spacing of approximately 0.325 nm observed in the HRTEM images is distinct from that of  $\beta\text{-Fe}_2\text{O}_3$  (see insets in Fig. S3B and C) and corresponds to the (002) crystal plane of  $\text{g-C}_3\text{N}_4$  in agreement with the literature [57].

Light absorption properties were studied by UV-vis spectroscopy. Fig. 6A displays the UV-vis absorption spectra of the

prepared materials obtained from the DR-spectra. The absorption edge of the pure  $\text{g-C}_3\text{N}_4$  material is around 450 nm while for the pure  $\beta\text{-Fe}_2\text{O}_3$  the absorbance is extended up to 650 nm. An obvious shift of the absorption band towards longer wavelengths is detected in the FCN-x series compared with the pure  $\text{g-C}_3\text{N}_4$  material. This is observed even for the sample with the lowest  $\beta\text{-Fe}_2\text{O}_3$  loading. These results clearly demonstrate that the red shift of the absorption edge in the  $\beta\text{-Fe}_2\text{O}_3/\text{g-C}_3\text{N}_4$  nanocomposites can be exclusively attributed to the presence of  $\beta\text{-Fe}_2\text{O}_3$ . An interesting observation is that the spectra of the FCN-x series could not be reproduced from a simple linear combination of the pure  $\text{g-C}_3\text{N}_4$  and  $\beta\text{-Fe}_2\text{O}_3$  spectra. This evidence supports the formation

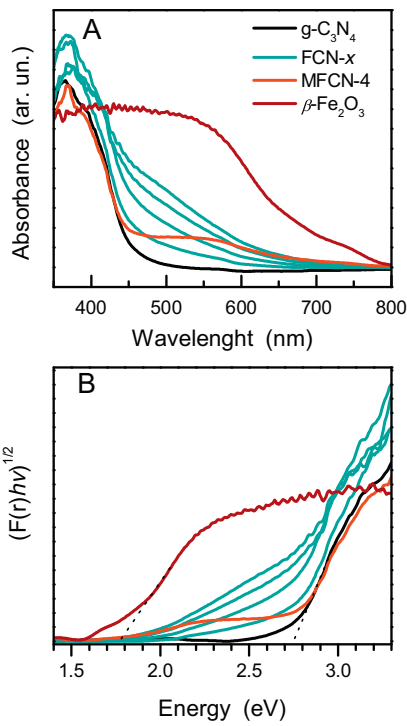


**Fig. 6.** UV-vis absorption spectra (A) and plots used to estimate band gap energies (B) considering the catalysts indirect semiconductors of the pure  $\text{g-C}_3\text{N}_4$  and  $\beta\text{-Fe}_2\text{O}_3$  and the nanocomposite  $\beta\text{-Fe}_2\text{O}_3/\text{g-C}_3\text{N}_4$  and MFCN-4.

of a hybrid heterostructure with appreciable interfacial interaction between the two components. On the contrary, the spectrum of the mechanically mixed MFCN-4 sample can be deconvoluted into the pure  $\text{g-C}_3\text{N}_4$  and  $\beta\text{-Fe}_2\text{O}_3$  UV-vis spectra.

The observed red shift in the hybrid nanocomposites (Fig. 6) gives rise to an appreciable decrease of the band gap energy ( $E_g$ ) in

the presence of  $\beta\text{-Fe}_2\text{O}_3$  but not in the mechanically mixed MFCN-4 sample (Table 1). The estimated band gap energy for the pure  $\text{g-C}_3\text{N}_4$  and  $\beta\text{-Fe}_2\text{O}_3$  are in close relation with the values reported in previous studies [11,12,55]. The increased absorption in the visible region of light and narrower band gap energies of the FCN-x hybrids compared to the reference  $\text{g-C}_3\text{N}_4$  can have a positive impact in photocatalysis.

### 3.2. Photocatalytic activity

The photocatalytic efficiency of the pure and hybrid materials prepared was evaluated against the photodegradation of organic dyes (MO and RhB) and phenol under both simulated solar and pure visible light irradiation. Fig. 7 presents the photocatalytic results for MO degradation together with the reference reactions. Control experiments in the absence of light or catalyst resulted in negligible degradation of MO, demonstrating that the observed decrease in the MO concentration is due a photocatalytic process. Using the pure  $\text{g-C}_3\text{N}_4$ , 57% of MO is degraded in 4 h. All  $\beta\text{-Fe}_2\text{O}_3$  containing hybrids presented superior activity than the reference  $\text{g-C}_3\text{N}_4$  under solar light irradiation. Among all catalysts, the hybrid containing 3.5% of  $\beta\text{-Fe}_2\text{O}_3$  (i.e. FCN-3) presented the highest activity. Further increase of the  $\beta\text{-Fe}_2\text{O}_3$  resulted to a slight decrease of the catalytic activity but still higher than the reference  $\text{g-C}_3\text{N}_4$ . In contrast to the hybrid materials, the mechanically mixed MFCN-4 sample presented approximately the same photoactivity as the reference  $\text{g-C}_3\text{N}_4$ . Among the different factors that can affect activity, the increased surface area in the FCN-x series can be ruled out. This is obvious when comparing the results of the FCN-1 vs. CN where surface area is almost doubled with only a negligible improvement in the photocatalytic activity.

The experimental data were well fitted with a first-order kinetic. The rate constants ( $k$ ) were obtained by fitting the data with the following equation:

$$\ln \left( \frac{C_0}{C} \right) = kt$$

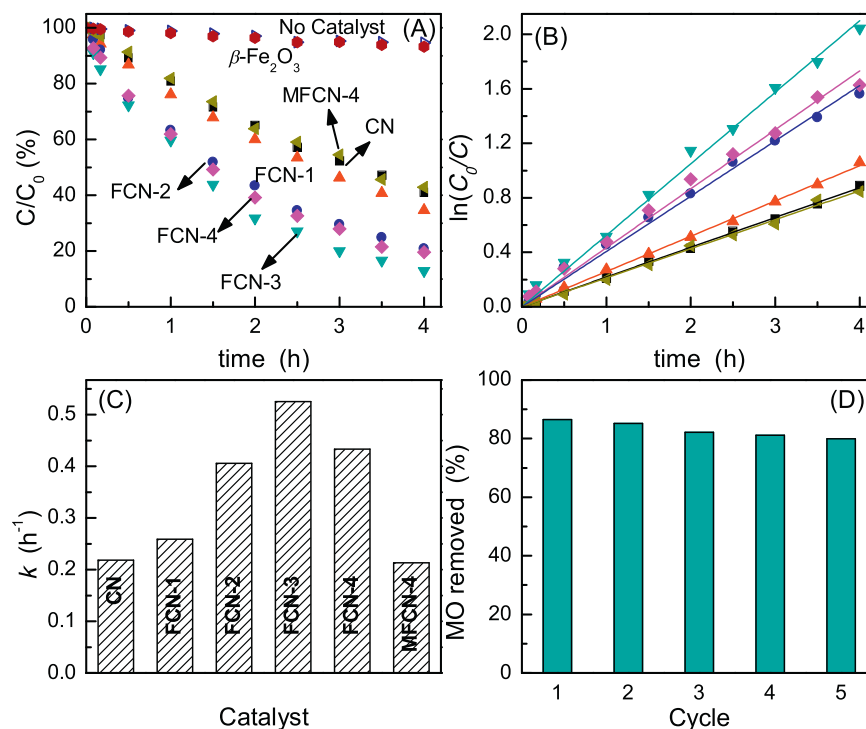


**Fig. 7.** Photocatalytic degradation of MO over the  $\text{g-C}_3\text{N}_4$ ,  $\beta\text{-Fe}_2\text{O}_3/\text{g-C}_3\text{N}_4$  and MFCN-4 photocatalysts under solar light irradiation (A), the corresponding first-order-kinetic plots (B) and the rate constants of MO degradation (C) and MO degradation efficiency after 4 h for three consecutive reaction processes for the FCN-3 photocatalyst (D).

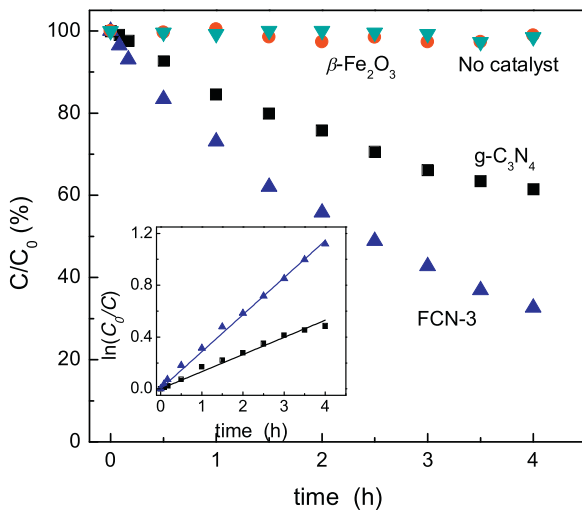


**Fig. 8.** Photocatalytic degradation of MO over the pure  $g\text{-C}_3\text{N}_4$ ,  $\beta\text{-Fe}_2\text{O}_3$  and the hybrid FCN-3 photocatalysts under pure visible light irradiation ( $\lambda > 420$  nm). Inset: first-order kinetic plots for the  $g\text{-C}_3\text{N}_4$  and FCN-3 photocatalysts.

where  $k$  is the apparent first-order rate constant ( $\text{min}^{-1}$ ),  $t$  is the irradiation time (min),  $C_0$  is the initial concentration and  $C$  the concentration at reaction time  $t$ . The linearity observed in the kinetic plots expressed as  $\ln(C_0/C)$  vs. Irradiation time ( $t$ ) (Fig. 7B) verified that the degradation follows first-order kinetics. The kinetic constant is 2.4 times higher in the FCN-3 than the pure  $g\text{-C}_3\text{N}_4$  sample. The rate constants extracted were 0.22 and  $0.21 \text{ h}^{-1}$  for the pure  $g\text{-C}_3\text{N}_4$  and the mechanical mixed MFCN-4 respectively and 0.26, 0.41, 0.53 and  $0.43 \text{ h}^{-1}$  for the FCN-1, -2, -3 and -4 nanohybrids, respectively (Fig. 7C). These data clearly show that the introduction of  $\beta\text{-Fe}_2\text{O}_3$  on the surface of  $g\text{-C}_3\text{N}_4$  is beneficial for photoactivity. However, enhanced photoactivity can be achieved only via the *in-situ* growth of  $\beta\text{-Fe}_2\text{O}_3$  nanoparticles on the  $g\text{-C}_3\text{N}_4$  surface.

Recycling reactions were performed on the most active catalyst (FCN-3) to evaluate the stability of the hybrid catalysts. The data presented in Fig. 7D reveal no apparent deactivation of the catalyst after three consecutive cycles, illustrating the excellent stability under the conditions of our experiment. It is important to underline that the ICP-AES analysis verified that the Fe concentration in the final solutions were always below the LOD limit ( $\sim 10 \mu\text{g L}^{-1}$ ). This value corresponds to an eventual leaching of 2.2% of Fe present in the FCN-3 sample. It should be mentioned that  $\alpha\text{-Fe}_2\text{O}_3$  is susceptible to detrimental photoleaching phenomena while  $\beta\text{-Fe}_2\text{O}_3$  is much more stable [45]. To further establish the stability of the prepared hybrids, the XRD pattern and FT-IR spectrum of the used FCN-4 catalyst was recorded presenting no obvious differences compared with the fresh CN and FCN-4 catalyst (Figure S4). These data further confirm the good stability of the present hybrid material.

The photoactivity of selected catalysts was also tested for the degradation of RhB and phenol. The data are presented in Figure S5. In both cases, photoactivity of the  $\beta\text{-Fe}_2\text{O}_3/g\text{-C}_3\text{N}_4$  hybrid is much higher than the pure  $g\text{-C}_3\text{N}_4$  reference catalyst. Since dye self-sensitized processes may occur in photocatalysis, of importance is the photoactivity against phenol that clearly demonstrates the absence of such phenomena in the present case. The observed enhanced photodegradation of RhB over MO by both the reference and the  $\beta\text{-Fe}_2\text{O}_3/g\text{-C}_3\text{N}_4$  hybrid catalysts may originate from dye sensitization phenomena that are more pronounced using RhB as the target pollutant [28].

Most importantly, in addition to the activity presented under simulated solar light, the prepared materials were proven active under pure visible light irradiation. Fig. 8 presents the time

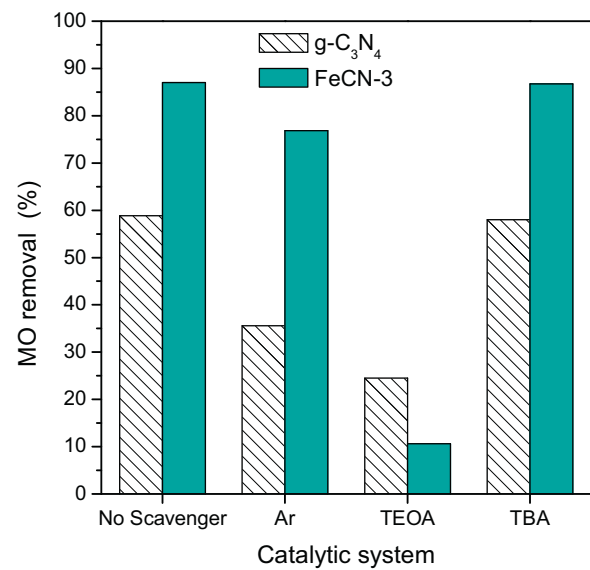


**Fig. 9.** Removal of MO by the reference  $g\text{-C}_3\text{N}_4$  and the FCN-3 nanocomposite after 4 h solar-light irradiation in the presence of various scavengers.

dependence of MO degradation and the plots used to estimate reaction rates for selected samples using pure visible light ( $>420$  nm). The FCN-3 hybrid presented higher activity compared to the pure reference materials. Comparing the catalytic results of our  $\beta\text{-Fe}_2\text{O}_3/g\text{-C}_3\text{N}_4$  hybrids with  $\text{Fe}_2\text{O}_3/g\text{-C}_3\text{N}_4$  photocatalysts reported in the literature containing  $\alpha$ - and  $\gamma\text{-Fe}_2\text{O}_3$  [14,27,38], the  $\beta\text{-Fe}_2\text{O}_3/g\text{-C}_3\text{N}_4$  hybrids present higher activity with respect to the enhancement factor over the reference photocatalyst used (as to the rate constant ( $k$ ) ratio). Specifically, an enhancement factor of 1.52 [14] and 1.8 [38] were reported over the reference material for  $g\text{-C}_3\text{N}_4$  functionalized with  $\alpha$ - and  $\gamma\text{-Fe}_2\text{O}_3$  respectively, while the corresponding value for FCN-3 is 2.4 and shows resemblance with Fe-doped  $g\text{-C}_3\text{N}_4$  [14].

### 3.3. Photocatalytic mechanism

To get insights into the reaction mechanism and to identify and assess the contribution of the active species, control experiments were conducted using scavengers for holes and free radicals over the most active FCN-3 and the reference  $g\text{-C}_3\text{N}_4$  sample. Triethanolamine (TEOA) and *tert*-butyl alcohol (TBA) were used as hole ( $h^+$ ) and hydroxyl radical ( $\text{OH}^\bullet$ ) scavengers, respectively [14,56]. To study the effect of superoxide radicals ( $\text{O}_2^{\bullet-}$ ) on photoactivity, control experiments under saturated argon atmosphere were performed, maintaining anaerobic environment throughout the reaction. The data are presented in Fig. 9, analyzing the MO degradation after 4 h of irradiation under simulated solar light. For both the pure  $g\text{-C}_3\text{N}_4$  and the FCN-3 hybrid, the photocatalytic degradation of MO is not affected by the presence of TBA. This clearly indicates that  $\text{OH}^\bullet$  have no effect on the photocatalytic reaction. Under saturated Ar atmosphere, a small decrease ( $\sim 10\%$ ) on reactivity is observed for the FCN-3, suggesting that dissolved  $\text{O}_2$  has a role in the photodegradation of MO most likely through the formation of  $\text{O}_2^{\bullet-}$ . However,  $\text{O}_2^{\bullet-}$  are not of significance in determining photoactivity of FCN-3 since photodegradation is only slightly diminished. On the contrary, degradation of MO was greatly suppressed in the case of FCN-3 when TEOA was used as scavenger. Therefore, photogenerated  $h^+$  are the dominant species determining photoactivity in the hybrid material in agreement with recent studies for MO, RhB and phenols degradation using  $g\text{-C}_3\text{N}_4$ -based composites [57]. In the pure  $g\text{-C}_3\text{N}_4$  material, catalytic degradation of MO is driven both from  $h^+$  and  $\text{O}_2^{\bullet-}$  while the impact

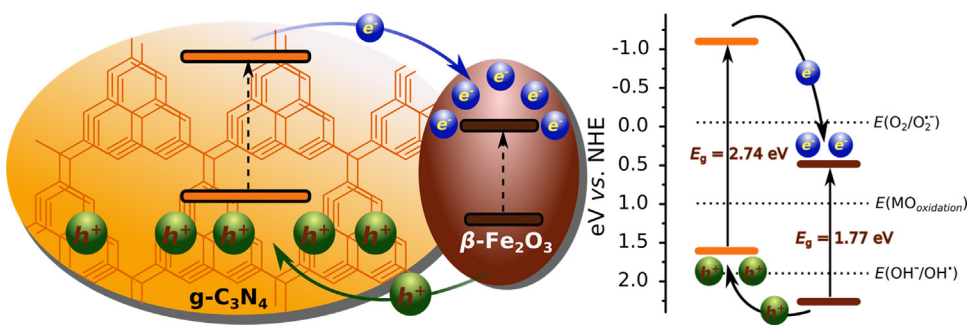


**Fig. 10.**  $\text{g-C}_3\text{N}_4$  and  $\beta\text{-Fe}_2\text{O}_3$  band edge positions and proposed charge transfer process in the  $\beta\text{-Fe}_2\text{O}_3/\text{g-C}_3\text{N}_4$  hybrids.

of  $\text{O}_2^{\bullet-}$  seems more prominent when compared with the hybrid  $\beta\text{-Fe}_2\text{O}_3/\text{g-C}_3\text{N}_4$  nanocomposites. These results also demonstrate that there is no contribution of a Fenton-type reaction in the photodegradation process of MO, considering that  $\text{OH}^{\bullet}$  and  $\text{O}_2^{\bullet-}$  are the main reactive species in the Fenton reaction [58].

These results indicate that photodegradation of MO is governed by different mechanisms in the pure  $\text{g-C}_3\text{N}_4$  and the hybrid  $\beta\text{-Fe}_2\text{O}_3/\text{g-C}_3\text{N}_4$  nanomaterials. For the pure  $\text{g-C}_3\text{N}_4$  the results are consistent with previous works [30,56]. However, for the  $\beta\text{-Fe}_2\text{O}_3/\text{g-C}_3\text{N}_4$  hybrids the results differ from previous studies performed on Fe-doped  $\text{g-C}_3\text{N}_4$  [13] or  $\text{g-C}_3\text{N}_4$  containing iron oxides [14,47]. Hu et al. reported recently that photodegradation of dyes is driven by both  $\text{O}_2^{\bullet-}$  and  $\text{OH}^{\bullet}$  using  $\alpha\text{-Fe}_2\text{O}_3/\text{g-C}_3\text{N}_4$  composites [14]. A similar mechanism was proposed for  $\text{Fe}_3\text{O}_4/\text{g-C}_3\text{N}_4$  hybrids [47] as well as for other  $\text{g-C}_3\text{N}_4$  composites [59]. However, in our  $\beta\text{-Fe}_2\text{O}_3/\text{g-C}_3\text{N}_4$  hybrid catalysts, photogenerated  $\text{h}^+$  are the primary active species for the photocatalytic oxidation of MO while  $\text{OH}^{\bullet}$  do not participate in the reaction.

The difference in catalytic activity between the mechanical mixed MFCN-4 catalyst, the pure  $\text{g-C}_3\text{N}_4$  and the *in-situ* synthesized nanocomposites may be related with the improved optical properties in the FCN- $x$  series (i.e. narrower  $E_g$ ), small sized and highly dispersed  $\beta\text{-Fe}_2\text{O}_3$  nanoparticles, avoiding the formation of agglomerates as evidenced by TEM. The tight interface formed between the two parts in the heterostructure should also be considered in the charge transfer process. Regarding this last factor, more information can be gained by the actual band structure of the heterostructure, e.g. the band edge position of  $\text{g-C}_3\text{N}_4$  and  $\beta\text{-Fe}_2\text{O}_3$ . The conduction and valence band (CB and VB) edges of  $\text{g-C}_3\text{N}_4$  lie approximately at  $-1.1$  V and  $+1.6$  V, respectively [11,12]. The VB and CB of  $\beta\text{-Fe}_2\text{O}_3$  were estimated by the following empirical equation [7]

$$E_{\text{VB}} = X - E_C + E_g$$

where  $E_{\text{VB}}$  is the VB edge potential,  $X$  the electronegativity of the semiconductor (which is the geometric mean of the electronegativity of the constituent atoms),  $E_C$  the energy of the free electron (4.5 eV on the hydrogen scale) and  $E_g$  is the band gap energy calculated from the UV-vis DR-spectra. For  $\beta\text{-Fe}_2\text{O}_3$  the absolute electronegativity is 5.87 eV. The conduction band edge potential ( $E_{\text{CB}}$ ) was obtained using

$$E_{\text{CB}} = E_{\text{VB}} - E_g$$

By applying this method, the CB and VB potentials of  $\beta\text{-Fe}_2\text{O}_3$  were calculated to be 0.49 and 2.25 eV. Although these may not be the absolute CB and VB potentials, the values extracted herein are in good agreement with the values reported in the literature for iron oxide polymorphs [27] and can be used as guides offering an estimation of the relative band edge positions.

A schematic diagram of the band structure in the nanocomposites together with the redox potential of reference reactions are

presented in Fig. 10. Under visible light irradiation, both  $\text{g-C}_3\text{N}_4$  and  $\beta\text{-Fe}_2\text{O}_3$  absorb photons with energy greater than their band gaps, resulting to the excitation of  $e^-$  to the CB while  $h^+$  remain in the VB. Based on the band structure of the heterojunction, photogenerated  $e^-$  in the CB of  $\text{g-C}_3\text{N}_4$  can be transferred to the less negative CB of  $\beta\text{-Fe}_2\text{O}_3$  while  $h^+$  are transferred from the VB of  $\beta\text{-Fe}_2\text{O}_3$  to that of  $\text{g-C}_3\text{N}_4$ . Therefore, the correctly aligned band edges of  $\beta\text{-Fe}_2\text{O}_3$  and  $\text{g-C}_3\text{N}_4$  suggest that efficient charge separation may occur through the strong interfacial interaction in the nanocomposites. The restriction of photogenerated  $e^-$  on the one side and  $h^+$  on the other *via* charge transfer due to the difference in the band edges reduces the recombination rate of  $e^-/h^+$  pairs and increases the abundance and stability of the photogenerated charge carriers in the hybrid nanomaterials [3]. This has an important impact in photoactivity as evidenced in Figs. 7 and 8 and S5.

Close inspection of the band levels in Fig. 10 reveals that the reduction potential of the CB  $e^-$  in  $\text{g-C}_3\text{N}_4$  are more negative while in  $\beta\text{-Fe}_2\text{O}_3$  are less negative than the normal potential of the  $\text{O}_2/\text{O}_2^{\bullet-}$  couple. Hence, CB  $e^-$  in  $\text{g-C}_3\text{N}_4$  can reduce  $\text{O}_2$  forming  $\text{O}_2^{\bullet-}$  while this cannot occur in  $\beta\text{-Fe}_2\text{O}_3$ . Therefore, it is not surprising the small impact of  $\text{O}_2^{\bullet-}$  in the photodegradation process in the case of the hybrid materials since  $e^-$  are effectively transfer from  $\text{g-C}_3\text{N}_4$  to  $\beta\text{-Fe}_2\text{O}_3$ . On the contrary,  $\text{O}_2^{\bullet-}$  contribute significantly when using the pure  $\text{g-C}_3\text{N}_4$ . Similarly, the oxidation potential of the photogenerated VB  $h^+$  in  $\text{g-C}_3\text{N}_4$  is not positive enough to generate  $\text{OH}^{\bullet}$  by direct oxidation of either the surface hydroxyl groups or adsorbed water molecules ( $E^0(\text{OH}^{\bullet}/\text{OH}) = 1.9$  V,  $E^0(\text{H}_2\text{O}_{\text{ads}}/\text{OH}^{\bullet}) = 2.7$  V vs. NHE) [60]. This is not the case for the VB  $h^+$  in  $\beta\text{-Fe}_2\text{O}_3$ . However, given that  $h^+$  are transferred from the VB of  $\beta\text{-Fe}_2\text{O}_3$  to  $\text{g-C}_3\text{N}_4$ ,  $\text{OH}^{\bullet}$  are not produced in the hybrid nanomaterials, explaining the results obtained using TBA as scavenger.  $\text{OH}^{\bullet}$  are not produced also *via*  $\text{O}_2$  multi-electron reduction process, in accordance with the low reduction potential of the conduction band  $e^-$  on  $\beta\text{-Fe}_2\text{O}_3$ , further verifying the catalytic results obtained using TBA as scavenger. The results obtained from the reference reactions using scavengers (e.g. no production of  $\text{OH}^{\bullet}$  and  $\text{O}_2^{\bullet-}$ ) verify the efficient charge separation in the hybrid materials as suggested by the CB and VB potential calculation. Finally, considering that the oxidation potential of MO is approximately 1 V (vs. NHE) [61], the potential of VB  $h^+$  in  $\text{g-C}_3\text{N}_4$  is high enough for direct oxidation of MO. Therefore, in the hybrid materials,  $h^+$  are the active species acting as direct oxidizing agents for MO and not producing  $\text{OH}^{\bullet}$ . In photocatalysis, usually different active species are generated (i.e.  $h^+$ ,  $e^-$ ,  $\text{OH}^{\bullet}$ ,  $\text{O}_2^{\bullet-}$ ). Herein, considering that only the photo-excited  $h^+$  participate in the catalytic mechanism when using the  $\beta\text{-Fe}_2\text{O}_3/\text{g-C}_3\text{N}_4$  hybrids indicate that these materials may find application in controlled sun-light driven catalytic reactions for selective organic synthesis.

Based on the above analysis, the enhanced photoactivity and the photocatalytic mechanism of MO degradation by the hybrid  $\beta\text{-Fe}_2\text{O}_3/\text{g-C}_3\text{N}_4$  nanomaterials are outlined in the scheme in Fig. 10.

Photogenerated VB  $h^+$  are the primary species determining photoactivity while the enhanced photoactivity is attributed to the efficient charge separation driven by the well-matched overlapping band-structures of  $\beta$ -Fe<sub>2</sub>O<sub>3</sub> and g-C<sub>3</sub>N<sub>4</sub>. Therefore,  $\beta$ -Fe<sub>2</sub>O<sub>3</sub> nanoparticles act simply as sensitizers and charge separators and do not participate in the degradation process or form reactive oxygen species.

#### 4. Conclusions

In summary, we have developed 2D hybrid nanomaterials consisting of Fe<sub>2</sub>O<sub>3</sub> at the metastable  $\beta$ -phase and g-C<sub>3</sub>N<sub>4</sub> via a facile *in-situ* growth strategy embedded in a solid state process. The  $\beta$ -Fe<sub>2</sub>O<sub>3</sub> enhances light absorption in the visible region, generating more charge carriers and simultaneously promoting charge transfer and separation due to the difference in the CB and VB energies. As a result, the hybrid  $\beta$ -Fe<sub>2</sub>O<sub>3</sub>/g-C<sub>3</sub>N<sub>4</sub> nanomaterials exhibit higher photocatalytic activity compared to the pure reference materials, coupled with a remarkable stability under working conditions. Photogenerated  $h^+$  were identified as the active species responsible for the dye degradation in the hybrid  $\beta$ -Fe<sub>2</sub>O<sub>3</sub>/g-C<sub>3</sub>N<sub>4</sub> while in the pure g-C<sub>3</sub>N<sub>4</sub> reference photoactivity is driven by both  $h^+$  and O<sub>2</sub><sup>•-</sup>.

#### Acknowledgements

Dr. Michele Melchionna and Dr. Matteo Crosera (University of Trieste) are acknowledged for assistance in the collection of TEM and ICP-AES analysis, respectively. Prof. Yiannis Deligianakis and Chris Daikopoulos (University of Ioannina, Greece) are fully acknowledged for the DR-UV-vis spectra. K.C.C. acknowledges the TALENTS FVG Programme for a Post-doctoral fellowship funded from the European Social Fund (Operational Programme 2007–2013, Objective 2 Regional Competitiveness and Employment, Axis 5 Transnational cooperation, TALENTS FVG Programme). The University of Trieste through the FRA2013 Project is fully acknowledged for financial support.

#### References

- [1] D. Ollis, P. Pichat, N. Serpone, *Appl. Catal. B* **99** (2010) 377.
- [2] A. Kubacka, M. Fernandez-Garcia, G. Colon, *Chem. Rev.* **112** (2012) 1555–1614.
- [3] K.C. Christoforidis, M. Fernandez-Garcia, *Catal. Sci. Technol.* (2016), <http://dx.doi.org/10.1039/C5CY00929D>.
- [4] Z. Yi, J. Ye, N. Kikugawa, T. Kako, S. Ouyang, H. Stuart-Williams, H. Yang, J. Cao, W. Luo, Z. Li, Y. Liu, R.L. Withers, *Nat. Mater.* **9** (2010) 559–564.
- [5] C. Cui, Y. Wang, D. Liang, W. Cui, H. Hu, B. Lu, S. Xu, X. Li, C. Wang, Y. Yang, *Appl. Catal. B* **158–159** (2014) 150–160.
- [6] K. Iwashina, A. Iwase, Y.H. Ng, R. Amal, A. Kudo, *J. Am. Chem. Soc.* **137** (2015) 604–607.
- [7] K.C. Christoforidis, A. Sengele, V. Keller, N. Keller, *ACS Appl. Mater. Interfaces* **7** (2015) 19324–19334.
- [8] H. Gu, Y. Yang, J. Tian, G. Shi, *ACS Appl. Mater. Interfaces* **5** (2013) 6762–6768.
- [9] M. Cargnello, M. Grzelczak, B. Rodriguez-Gonzalez, Z. Syrgiannis, K. Bakhmutsky, V. La Parola, L.M. Liz-Marzan, R.J. Gorte, M. Prato, P. Fornasiero, *J. Am. Chem. Soc.* **134** (2012) 11760–11766.
- [10] K.C. Christoforidis, S.J.A. Figueroa, M. Fernandez-Garcia, *Appl. Catal. B* **117–118** (2012) 310–316.
- [11] Z. Zhao, Y. Sun, F. Dong, *Nanoscale* **7** (2015) 15–37.
- [12] X.C. Wang, K. Maeda, A. Thomas, K. Takanabe, G. Xin, J.M. Carlsson, K. Domen, M. Antonietti, *Nat. Mater.* **8** (2009) 76–80.
- [13] S. Tonda, S. Kumar, S. Kandula, V. Shanker, *J. Mater. Chem. A* **2** (2014) 6772–6780.
- [14] S. Hu, R. Jin, G. Lu, D. Liub, J. Gui, *RSC Adv.* **4** (2014) 24863–24869.
- [15] Z. Ding, X. Chen, M. Antonietti, X. Wang, *ChemSusChem* **4** (2011) 274–281.
- [16] X.F. Chen, J.S. Zhang, X.Z. Fu, M. Antonietti, X.C. Wang, *J. Am. Chem. Soc.* **131** (2009) 11658–11659.
- [17] G.G. Zhang, M.W. Zhang, X.X. Ye, X.Q. Qiu, S. Lin, X.C. Wang, *Adv. Mater.* **26** (2014) 805–809.
- [18] S.C. Yan, Z.S. Li, Z.G. Zou, *Langmuir* **26** (2010) 3894–3901.
- [19] Y.J. Zhang, T. Mori, J.H. Ye, M. Antonietti, *J. Am. Chem. Soc.* **132** (2010) 6294–6295.
- [20] F. Su, S. Mathew, G. Lipner, X. Fu, M. Antonietti, S. Blechert, X. Wang, *J. Am. Chem. Soc.* **132** (2010) 16299–16301.
- [21] L. Huang, H. Xu, Y. Li, H. Li, X. Cheng, J. Xia, Y. Xu, G. Cai, *Dalton Trans.* **42** (2013) 8606–8616.
- [22] S. Bai, X. Wang, C. Hu, M. Xie, J. Jiang, Y. Xiong, *Chem. Commun.* **50** (2014) 6094–6097.
- [23] Y. Di, X. Wang, A. Thomas, M. Antonietti, *ChemCatChem* **2** (2010) 834–838.
- [24] J.H. Sun, J.S. Zhang, M.Z. Zhang, M. Antonietti, X.Z. Fu, X.C. Wang, *Nat. Commun.* (2012) 1139–1144.
- [25] Y. Zhao, F. Zhao, X. Wang, C. Xu, Z. Zhang, G. Shi, L. Qu, *Angew. Chem. Int. Ed.* **53** (2014) 1–7.
- [26] 3R.Y. Zheng, L. Lin, X. Ye, F., Guo, X. Wang, *Angew. Chem. Int. Ed.* **53** (2014) 11926–11930.
- [27] J. Theerthagiri, R.A. Senthil, A. Priya, J. Madhavan, R.J.V. Michael, M. Ashokkumar, *RSC Adv.* **4** (2014) 38222–38229.
- [28] J. Fu, B.B. Chang, Y.L. Tian, F.N. Xi, X.P. Dong, *J. Mater. Chem. A* **1** (2013) 3083–3090.
- [29] Y.D. Hou, A.B. Laursen, J.S. Zhang, G.G. Zhang, Y.S. Zhu, X.C. Wang, *Angew. Chem. Int. Ed.* **52** (2013) 3621–3625.
- [30] Y. He, L. Zhang, X. Wang, Y. Wu, H. Lin, L. Zhao, W. Weng, H. Wand, M. Fan, *RSC Adv.* **4** (2014) 13610–13619.
- [31] K.-I. Katsumata, R. Motoyoshi, N. Matsushita, K. Okada, *J. Hazard. Mater.* **260** (2013) 475–482.
- [32] X. Ye, Y. Cui, X. Qiu, X. Wang, *Appl. Catal. B* **152–153** (2014) 383–389.
- [33] X. Ye, Y. Cui, X. Wang, *ChemSusChem* **7** (2014) 738–742.
- [34] F. Dong, Z. Zhao, Y. Sun, Y. Zhang, S. Yan, Z. Wu, *Environ. Sci. Technol.* **49** (2015) 12432–12440.
- [35] Q. Gu, Z. Gao, H. Zhao, Z. Lou, Y. Liao, C. Xue, *RSC Adv.* **5** (2015) 49317–49325.
- [36] Y. Liao, S. Zhu, J. Ma, Z. Sun, C. Yin, C. Zhu, X. Lou, D. Zhang, *ChemCatChem* **6** (2014) 3419–3425.
- [37] J. Mao, T. Peng, X. Zhang, K. Li, L. Yea, L. Zan, *Catal. Sci. Technol.* **3** (2013) 1253–1260.
- [38] S. Ye, L.G. Qiu, Y.P. Yuan, Y.J. Zhu, J. Xia, J.F. Zhu, *J. Mater. Chem. A* **1** (2013) 3008–3015.
- [39] S. Zhang, Y. Yang, Y. Guo, W. Guo, M. Wang, Y. Gu, M. Huo, *J. Hazard. Mater.* **261** (2013) 235–245.
- [40] M. Li, L. Zhang, X. Fan, Y. Zhou, M. Wu, J. Shi, *J. Mater. Chem. A* **3** (2015) 5189–5196.
- [41] Y. Hong, Y. Jiang, C. Li, W. Fan, X. Yan, M. Yan, W. Shi, *Appl. Catal. B* **180** (2016) 663–673.
- [42] K. Sivula, F. Le Formal, M. Gratzel, *ChemSusChem* **4** (2011) 432–449.
- [43] T. Danno, D. Nakatsuka, Y. Kusano, H. Asaoka, M. Nakanishi, T. Fujii, Y. Ikeda, J. Takada, *Cryst. Growth Des.* **13** (2013) 770–774.
- [44] J. Tucek, R. Zboril, A. Namai, S.-I. Ohkoshi, *Chem. Mater.* **22** (2010) 6483–6505.
- [45] G. Carraro, C. Maccato, A. Gasparotto, T. Montini, S. Turner, O.I. Lebedev, V. Gombac, G. Adami, G. Van Tendeloo, D. Barreca, P. Fornasiero, *Adv. Funct. Mater.* **24** (2014) 372–378.
- [46] G. Carraro, A. Gasparotto, C. Maccato, V. Gombac, F. Rossi, T. Montini, D. Peeters, E. Bontempi, C. Sada, D. Barreca, P. Fornasiero, *RSC Adv.* **4** (2014) 32174–32179.
- [47] S. Kumar, T. Surendar, B. Kumar, A. Baruah, V. Shankar, *J. Phys. Chem. C* **117** (2013) 26135–26143.
- [48] R.C. Pawar, Y. Pyo, S.H. Ahn, C.S. Lee, *Appl. Catal. B* **176–177** (2015) 654–666.
- [49] X. Ye, Y. Cui, X. Qiu, X. Wang, *Appl. Catal. B* **152–153** (2014) 383–389.
- [50] X. Ye, Y. Cui, X. Wang, *ChemSusChem* **7** (2014) 738–742.
- [51] S.C. Warren, K. Voitchovsky, H. Dotan, C.M. Leroy, M. Cornuz, F. Stellacci, C. Hebert, A. Rothschild, M. Gratzel, *Nat. Mater.* **12** (2013) 842–849.
- [52] S.C. Yan, Z.S. Li, Z.G. Zou, *Langmuir* **25** (2009) 10397–10401.
- [53] Y. Liao, W. Que, P. Zhong, J. Zhang, Y. He, *ACS Appl. Mater. Interfaces* **3** (2011) 2800–2804.
- [54] X.C. Wang, A. Thomas, X.Z. Fu, M. Antonietti, *Adv. Mater.* **21** (2009) 1609–1612.
- [55] C.-W. Lee, K.-W. Lee, J.-S. Lee, *Mater. Lett.* **62** (2008) 2664–2666.
- [56] H. Ji, F. Chang, X. Hu, W. Qin, J. Shen, *Chem. Eng. J.* **218** (2013) 183–190.
- [57] J. Di, J. Xia, S. Yin, H. Xu, L. Xu, Y. Xu, M. He, H. Li, *J. Mater. Chem. A* **2** (2014) 5340–5351.
- [58] J.J. Pignatello, E. Oliveros, A. MacKay, *Crit. Rev. Environ. Sci. Technol.* **36** (2006) 1–84.
- [59] J. Di, J. Xia, S. Yin, H. Xu, L. Xu, Y. Xu, M. He, H. Li, *J. Mater. Chem. A* **2** (2014) 5340–5351.
- [60] Y. Zheng, J. Liu, J. Liang, M. Jaroniec, S.Z. Qiao, *Energy Environ. Sci.* **5** (2012) 6717–6731.
- [61] A. Zille, P. Ramalho, T. Tzanov, R. Millward, V. Aires, M.H. Cardoso, M.T. Ramalho, G.M. Gubitz, A. Cavaco-Paulo, *Biotechnol. Prog.* **20** (2004) 1588–1592.